

Small-Signal Modeling and Stability Analysis of a Droop-Controlled Grid-Forming Inverter

Jack S. Bryant, Brendan McGrath, Lasantha Meegahapola, and Peter Sokolowski

School of Engineering

RMIT University

Melbourne, VIC, Australia

{jack.bryant, brendan.mcgrath, lasantha.meegahapola, peter.sokolowski}@rmit.edu.au

Abstract—Grid-forming inverters present a promising control philosophy for inverter-dominated power grids. However, further research is required to better understand the modeling and control of such devices, yielding design and performance improvements alike. This paper systematically develops a small-signal model predicated upon a state-space framework, accurately capturing dynamics associated with the current and voltage regulators, droop controller, modulation scheme, *LCL* filter, and grid connection. Participation factor analysis compares and contrasts the modal characteristics of grid-forming and grid-feeding inverter topologies, with the main differences observed in the states contributing to the fastest modes (eigenvalues). Moreover, small-signal analysis of the current and voltage regulators' proportional gains demonstrates the latter's significance concerning the grid-forming inverter's stability. Time-domain simulations validate the small-signal model's predictions.

Index Terms—droop control, grid-forming inverter, participation factors, small-signal stability.

I. INTRODUCTION

Power electronic inverters are now forming the backbone of modern power grids as an interface between renewable energy sources, such as wind and solar photovoltaic (PV) systems, and the electricity network at transmission and distribution levels. Grid-forming (GFM) control is a nascent inverter control philosophy (compared to the well-known grid-following control), allowing an inverter to set the voltage and frequency reference for a power system [1]. Such inverters can operate either grid-connected or in a standalone fashion independent of the main power grid. In contrast, grid-following controls cannot autonomously operate as they depend upon estimating the frequency of the power grid (typically using a phase-locked loop).

GFM inverter controls provide a faster response than their grid-feeding counterparts, with lower droop gains improving stability [2]. Moreover, GFM inverters increase small-signal stability under weak grid conditions [3]. At the same time, the steady-state operating region remains unchanged, providing a valuable option to overcoming issues related to low short-circuit ratios in renewable-rich areas of the grid. Simultaneously optimizing the many control parameters of GFM inverters has been shown to yield a very stable system, characterized by eigenvalues well inside the left half-

plane (LHP) [4]. Shaping the transient response of a droop-controlled GFM inverter using the DC link voltage also shows promising stability improvements [5]. A new method for modeling inverter-based generators, termed impedance circuit modeling, has recently been applied to a droop-controlled GFM inverter scheme, yielding a more granulated description of the control architecture compared to traditional impedance modeling techniques [6].

This work's contribution is threefold:

- 1) We provide an accurate mathematical description of a droop-controlled GFM inverter by capturing the dynamics associated with the *LCL* filter, voltage regulator, current regulator, droop control scheme, and pulse width modulation inclusive of the system's transport delays.
- 2) The modal analysis illustrates some of the main differences between the dynamics of GFM and grid-feeding inverter topologies.
- 3) The small-signal analysis demonstrates the significance of the voltage regulator's proportional gain on the GFM inverter's stability.

II. MATHEMATICAL MODEL

We consider a droop-controlled GFM voltage source inverter, such as that shown in Fig. 1, comprising inner loop current and voltage regulators and an outer loop droop control scheme. Only the basic GFM control architecture is considered in this work. We model the system in the nominal grid's synchronous reference frame (SRF), i.e., concerning the SRF of an arbitrary GFM inverter (without droop control), where $\omega^* = \omega_0$ (refer Fig. 2).

A. Nonlinear State-Space Formulation

The inverter's behaviour is governed by a set of states \mathcal{S} , a set of reference inputs \mathcal{U} , a set of disturbance inputs \mathcal{E} , and a set of outputs \mathcal{Y} . The grid-connected inverter is described using a system of nonlinear differential-algebraic equations (DAEs) of the form

$$\dot{\mathbf{x}}_{inv} = \mathbf{f}(\mathbf{x}_{inv}, \mathbf{u}_{inv}, \mathbf{e}_{inv}) \quad (1)$$

$$\mathbf{y}_{inv} = \mathbf{g}(\mathbf{x}_{inv}, \mathbf{u}_{inv}, \mathbf{e}_{inv}) \quad (2)$$

where $\mathbf{x}_{inv} \in \mathbb{R}^{|\mathcal{S}|}$, $\mathbf{u}_{inv} \in \mathbb{R}^{|\mathcal{U}|}$, $\mathbf{e}_{inv} \in \mathbb{R}^{|\mathcal{E}|}$, and $\mathbf{y}_{inv} \in \mathbb{R}^{|\mathcal{Y}|}$, are the state, input, disturbance, and output vectors, respectively, and $\mathbf{f} : \mathbb{R}^{|\mathcal{S}|+|\mathcal{U}|+|\mathcal{E}|} \mapsto \mathbb{R}^{|\mathcal{S}|}$ and

This work was supported in part by Australian Research Council Discovery Project DP180103200.

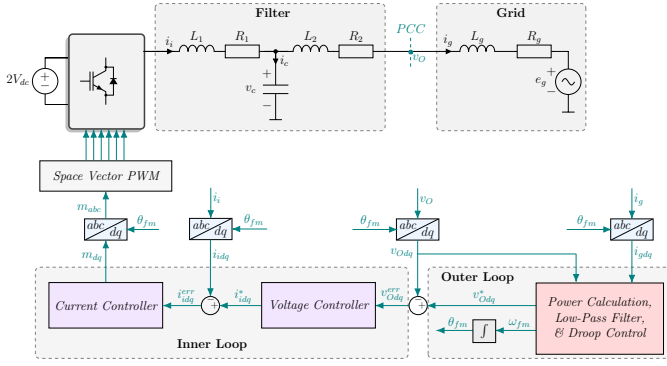


Fig. 1. Droop-controlled grid-forming voltage source inverter.

$g : \mathbb{R}^{|S|+|U|+|E|} \mapsto \mathbb{R}^{|Y|}$. The dynamics of the LCL filter are described by six differential equations, viz.

$$\dot{i}_{id} = \frac{V_{dc}}{L_1} m'_d - \frac{1}{L_1} v_{cd} - \frac{R_1}{L_1} i_{id} + \omega_0 i_{iq} \quad (3)$$

$$\dot{i}_{iq} = \frac{V_{dc}}{L_1} m'_q - \frac{1}{L_1} v_{cq} - \frac{R_1}{L_1} i_{iq} - \omega_0 i_{id} \quad (4)$$

$$\dot{i}_{gd} = \frac{1}{L_2} v_{cd} - \frac{1}{L_2} v_{Od} - \frac{R_2}{L_2} i_{gd} + \omega_0 i_{gq} \quad (5)$$

$$\dot{i}_{gq} = \frac{1}{L_2} v_{cq} - \frac{1}{L_2} v_{Oq} - \frac{R_2}{L_2} i_{gq} - \omega_0 i_{gd} \quad (6)$$

$$\dot{v}_{cd} = \frac{1}{C_f} i_{id} - \frac{1}{C_f} i_{gd} + \omega_0 v_{cq} \quad (7)$$

$$\dot{v}_{cq} = \frac{1}{C_f} i_{iq} - \frac{1}{C_f} i_{gq} - \omega_0 v_{cd} \quad (8)$$

where $i_{idq}, i_{gdq} \in \mathbb{R}^2$ are the inverter-side and grid-side currents, $v_{cdq}, v_{Odq} \in \mathbb{R}^2$ are the filter capacitor and PCC voltages, and $m_{dq} \in \mathbb{R}^2$ is the implemented modulation signal. Moreover, $L_1, R_1 \in \mathbb{R}_{>0}$ are the inverter-side filter inductance and resistance, $L_2, R_2 \in \mathbb{R}_{>0}$ are the grid-side filter inductance and resistance, and $C_f \in \mathbb{R}_{>0}$ is the filter capacitance, as given in Fig. 1. Note that the inverter is averaged over one switching period, thus its output voltage is represented by $m'_{dq} V_{dc}$, where $V_{dc} \in \mathbb{R}_{>0}$ is half of the total DC link voltage. Furthermore, the PCC voltage (in the nominal grid's SRF) is developed as a linear combination of the states and input disturbances, such that

$$v_{Odq} = \frac{L_2}{L_2 + L_g} e_{gdq} + \frac{L_2 R_g - L_g R_2}{L_2 + L_g} i_{gdq} + \frac{L_g}{L_2 + L_g} v_{cdq}. \quad (9)$$

where $e_{gdq} \in \mathbb{R}^2$ represents the grid voltage.

The outer loop droop control scheme is shown in Fig. 3. The inverter's measured instantaneous active and reactive power is given by

$$\tilde{p}^{fm} = \frac{3}{2} \left(v_{Od}^{fm} i_{gd}^{fm} + v_{Oq}^{fm} i_{gq}^{fm} \right) \quad (10)$$

$$\tilde{q}^{fm} = \frac{3}{2} \left(v_{Od}^{fm} i_{gq}^{fm} - v_{Oq}^{fm} i_{gd}^{fm} \right). \quad (11)$$

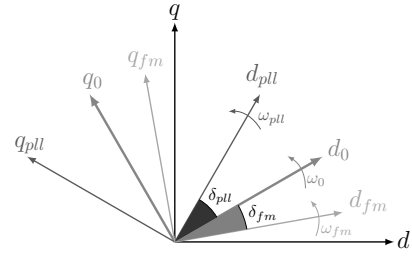


Fig. 2. Alignment of droop-controlled GFM (ω_{fm}) and grid-feeding (ω_{pll}) inverter SRFs to the SRF of an arbitrary GFM inverter without droop (ω_0).

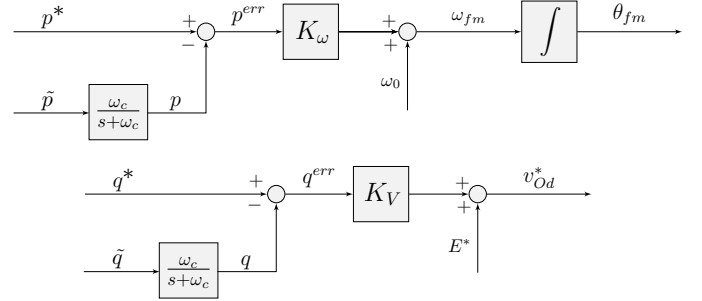


Fig. 3. Outer loop droop controllers.

where $\tilde{p}^{fm}, \tilde{q}^{fm} \in \mathbb{R}$ are the unfiltered active and reactive power measurements, respectively, $v_{Odq}^{fm}, i_{gdq}^{fm} \in \mathbb{R}^2$ are the PCC voltage and grid-side current aligned with the droop-controlled GFM inverter's SRF, i.e.,

$$v_{Od}^{fm} = v_{Od} \cos(\delta_{fm}) + v_{Oq} \sin(\delta_{fm}) \quad (12)$$

$$v_{Oq}^{fm} = -v_{Od} \sin(\delta_{fm}) + v_{Oq} \cos(\delta_{fm}) \quad (13)$$

$$i_{gd}^{fm} = i_{gd} \cos(\delta_{fm}) + i_{gq} \sin(\delta_{fm}) \quad (14)$$

$$i_{gq}^{fm} = -i_{gd} \sin(\delta_{fm}) + i_{gq} \cos(\delta_{fm}) \quad (15)$$

where

$$\delta_{fm} = \int K_\omega (p^* - p) dt \quad (16)$$

corresponds to the phase angle difference between the nominal grid and inverter SRFs (i.e., $\theta_{fm} - \theta_0$). Note that $K_\omega = (\omega_0 / S_{base}) \times \Delta\omega\%$, where S_{base} and ω_0 are the base values for the inverter's apparent power and nominal angular frequency. A low-pass filter is employed to remove unwanted harmonic content in the instantaneous power signals, whose dynamics are described by

$$\dot{p} = \omega_c (\tilde{p}^{fm} - p) \quad (17)$$

$$\dot{q} = \omega_c (\tilde{q}^{fm} - q) \quad (18)$$

where $p, q \in \mathbb{R}$ are the filtered active and reactive power measurements, respectively. The reference signals for the inner control loop and SRF transformations are then given by

$$\omega_{fm} = \omega_0 + K_\omega (p^* - p) \quad (19)$$

$$v_{Od}^{*fm} = E^* + K_V (q^* - q) \quad (20)$$

$$v_{Oq}^{*fm} = 0 \quad (21)$$

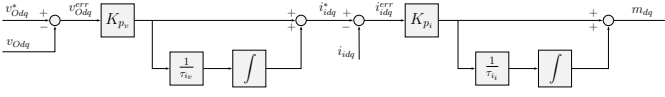


Fig. 4. Inner loop voltage and current regulators.

where $\omega_{fm}, \omega_0 \in \mathbb{R}_{>0}$ are the reference and nominal angular frequency, respectively, $v_{Odq}^{*fm} \in \mathbb{R}^2$ are the dq -axis PCC voltage references, and $E^* \in \mathbb{R}_{>0}$ is the nominal voltage reference. Moreover, $K_\omega, K_V \in \mathbb{R}_{>0}$ are the droop gains for the P - ω and Q - V channels, respectively, where $K_V = (V_{base}/S_{base}) \times \Delta V\%$. V_{base} and $\Delta V\%$ are the base voltage and desired droop in percent.

Fig. 4 illustrates the inner loop voltage and current regulators. The inverter-side current references (i_{idq}^{*fm}) generated by the voltage regulator are given by

$$i_{idq}^{*fm} = K_{pv} \left(v_{Odq}^{*fm} - v_{Odq}^{fm} \right) + \frac{K_{pv}}{\tau_{iv}} x_{dv}^v \quad (22)$$

where the dynamic states (x_{dv}^v) are formed as

$$\dot{x}_d^v = v_{Od}^{*fm} - v_{Od} \cos(\delta_{fm}) - v_{Oq} \sin(\delta_{fm}) \quad (23)$$

$$\dot{x}_q^v = v_{Oq}^{*fm} + v_{Od} \sin(\delta_{fm}) - v_{Oq} \cos(\delta_{fm}). \quad (24)$$

Moreover, the undelayed modulation commands (m_{dq}^{fm}) are

$$m_{dq}^{fm} = K_{pi} \left(i_{idq}^{*fm} - i_{idq}^{fm} \right) + \frac{K_{pi}}{\tau_{ii}} x_{di}^i \quad (25)$$

where we describe the current regulator states (x_{di}^i) by

$$\dot{x}_d^i = i_{id}^{*fm} - i_{id} \cos(\delta_{fm}) - i_{iq} \sin(\delta_{fm}) \quad (26)$$

$$\dot{x}_q^i = i_{iq}^{*fm} + i_{id} \sin(\delta_{fm}) - i_{iq} \cos(\delta_{fm}). \quad (27)$$

The implemented (delayed) modulation signals aligned to the inverter's SRF are

$$m_{dq}'^{fm} = x_{dq}' - m_{dq}^{fm}. \quad (28)$$

Thus, the transport delay states are given by [7]

$$\dot{x}_{dq}' = -\frac{2}{T_d} x_{dq}' + \frac{4}{T_d} m_{dq}^{fm}. \quad (29)$$

Note that as the implemented modulation signals in (3) and (4) are in the nominal grid's SRF, we need to rotate (28) by the angle difference between the two SRFs, viz.

$$m_d' = m_d'^{fm} \cos(\delta_{fm}) - m_q'^{fm} \sin(\delta_{fm}) \quad (30)$$

$$m_q' = m_d'^{fm} \sin(\delta_{fm}) + m_q'^{fm} \cos(\delta_{fm}). \quad (31)$$

B. Small-Signal Formulation

The resulting small-signal model is of the form

$$\Delta \dot{\mathbf{x}}_{inv} = A \Delta \mathbf{x}_{inv} + B \Delta \mathbf{u}_{inv} + \Gamma \Delta \mathbf{e}_{inv} \quad (32)$$

$$\Delta \mathbf{y}_{inv} = C \Delta \mathbf{x}_{inv} + D \Delta \mathbf{u}_{inv} + \Lambda \Delta \mathbf{e}_{inv} \quad (33)$$

where $A = \frac{\partial \mathbf{f}}{\partial \mathbf{x}_{inv}}$, $B = \frac{\partial \mathbf{f}}{\partial \mathbf{u}_{inv}}$, $\Gamma = \frac{\partial \mathbf{f}}{\partial \mathbf{e}_{inv}}$, $C = \frac{\partial \mathbf{g}}{\partial \mathbf{x}_{inv}}$, $D = \frac{\partial \mathbf{g}}{\partial \mathbf{u}_{inv}}$, $\Lambda = \mathbf{0}$, and $\Delta \mathbf{x}_{inv}$, $\Delta \mathbf{u}_{inv}$, $\Delta \mathbf{e}_{inv}$, and $\Delta \mathbf{y}_{inv}$ are small-signal perturbations in the state, input,

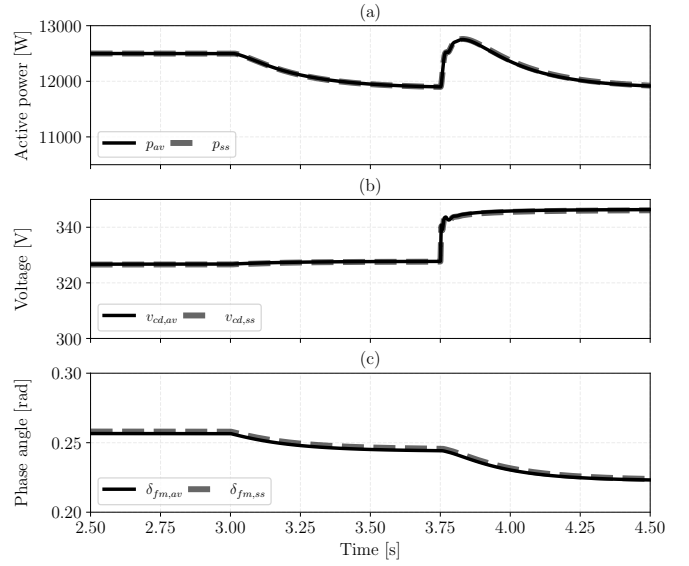


Fig. 5. Small-signal and averaged inverter model comparisons in response to a 5% decrease in p^* at $t = 3$ s followed by a 4% increase in E^* at 3.75 s. (a) Active power. (b) d -axis filter capacitor voltage. (c) SRF phase angle difference.

disturbance, and output vectors, respectively, which are formulated as follows:

$$\Delta \mathbf{x}_{inv} = \begin{bmatrix} \Delta x_{dq}^v & \Delta x_{dq}^i & \Delta x_{dq}' & \Delta i_{dq} & \Delta i_{gdq} \\ \Delta v_{cdq} & \Delta \delta_{fm} & \Delta p & \Delta q \end{bmatrix}^T \in \mathbb{R}^{15} \quad (34)$$

$$\Delta \mathbf{u}_{inv} = [\Delta p^* \quad \Delta q^* \quad \Delta E^* \quad \Delta v_{Oq}^*]^T \in \mathbb{R}^4 \quad (35)$$

$$\Delta \mathbf{e}_{inv} = [\Delta e_{gd} \quad \Delta e_{gq}]^T \in \mathbb{R}^2. \quad (36)$$

The small-signal model is developed about a steady-state operating point corresponding to the equilibrium solution of (1), i.e., $\mathbf{f}(\mathbf{x}_{inv}, \mathbf{u}_{inv}, \mathbf{e}_{inv}) = \mathbf{0}$. We do not show the full small-signal formulation in this paper, owing to space constraints.

C. Validation of Mathematical Model

Last, we validate the nonlinear state-space and small-signal formulations using the PSIM software package by encoding the analytic expressions of the mathematical models and comparing each time-domain trajectory to an averaged inverter model under steady-state and perturbed conditions. Fig. 5 demonstrates a subset of small-signal and averaged inverter model responses to perturbations in the reference inputs p^* and E^* . Note that the time-domain trajectories are in good agreement.

III. SMALL-SIGNAL STABILITY

We now consider the small-signal stability of the droop-controlled GFM inverter given the controller parameters and operating points detailed in Table I, with the filter parameters and inner/outer loop control gains based on the methodology outlined in [6]. The operating point's short-circuit ratio (SCR) corresponds to approximately 3.9.

TABLE I
SYSTEM PARAMETERS AND OPERATING POINTS.

Parameter	Value	Parameter	Value
V_{dc}	325 V	C_f	328 μF
L_1	1.3 mH	R_1	0.01 Ω
L_2	0.3 mH	R_2	0.03 Ω
L_g	11 mH	R_g	0.69 Ω
K_{p_i}	0.0125 A^{-1}	τ_{i_i}	0.4138 s
K_{p_v}	0.0154 Ω	τ_{i_v}	79.6 μs
K_ω	0.0005 rad/sW^{-1}	K_v	0.0014 V/VAr
T_d	75 μs	f_{sw}	10 kHz
ω_0	100 π rad/s	ω_c	10 π rad/s
p^*	11250 W	q^*	0 VAr
E^*	240 $\sqrt{2}$ V	v_{oq}^*	0 V
e_{gd}	339.4 V	e_{gq}	53 mV
S_{base}	12 500 V A	V_{base}	240 $\sqrt{2}$ V

A. Modal Analysis

First, we perform modal analysis through computation of the GFM inverter's participation factors $p_{k,i}$, which express the contribution of the k^{th} state in the i^{th} mode [8], viz.

$$p_{k,i} = \psi_{i,k} \phi_{k,i} \quad (37)$$

where $\phi_{k,i}$ is the k^{th} row element of the right eigenvector ϕ_i and $\psi_{i,k}$ is the k^{th} column element of the left eigenvector ψ_i . Fig. 6 illustrates the resulting participation matrix given the system parameters in Table I and the corresponding eigenvalues in Table II. Note that the transport delay (x'_{dq}) and inverter-side current (i_{idq}) states contribute the most to the system's slowest modes, whereas the moderately fast modes are mainly affected by the LCL filter (i_{gdq} , v_{cdq}) and the voltage regulator (x^v_{dq}) states, respectively. The fastest modes are predominantly influenced by the active and reactive power (p , q), the SRF angle difference (δ_{fm}), and the current regulator (x^i_{dq}) states.

Moreover, Table III compares the participation factors of the GFM inverter (Fig. 1) to the grid-feeding inverter topology presented in [9], including and excluding droop control schemes. Note, we consider the same controller, LCL filter, and grid impedance parameters for each inverter topology as given in Table I. Observe that the modulation transport delay and inverter-side current states dominate the slowest modes of each inverter system (x'_{dq} , i_{idq}). Moreover, the LCL filter states contribute the most to the moderately fast modes. However, the main modal differences between the inverter topologies occur in the fastest modes. For the GFM inverters, the current regulator states (x^i_{dq}) contribute the most; the addition of the droop controller produces relatively high contributions from the SRF angle difference (δ_{fm}) and active/reactive powers (p , q). For the grid-feeding inverter, the fastest modes are mainly affected by the inverter-side current references (i_{dq}^*), the current regulator (x_{dq}^{PI}), and the phase-locked loop (γ_{pli}). Note that applying the optimized gain methodology presented in [10] to the grid-feeding inverter given the filter parameters in Table I yields an unstable system, which suggests an alternative design methodology may be required to design a GFM inverter optimally.

TABLE II
EIGENVALUES FOR THE DROOP-CONTROLLED GFM SYSTEM.

	Eigenvalue ($\sigma \pm j\omega$)	Oscillation frequency (Hz)	Damping ratio
$\lambda_{1,2}$	$-19189 \pm j156.08$	24.841	0.9999
$\lambda_{3,4}$	$-3726.8 \pm j465.77$	74.129	0.9923
$\lambda_{5,6}$	$-422.59 \pm j1162.7$	185.04	0.3416
$\lambda_{7,8}$	$-256.77 \pm j740.10$	117.79	0.3278
$\lambda_{9,10}$	$-68.287 \pm j207.96$	33.097	0.3120
$\lambda_{11,12}$	$-14.930 \pm j23.468$	3.7351	0.5368
λ_{13}	-25.519	0	1
λ_{14}	-2.4269	0	1
λ_{15}	-2.4236	0	1

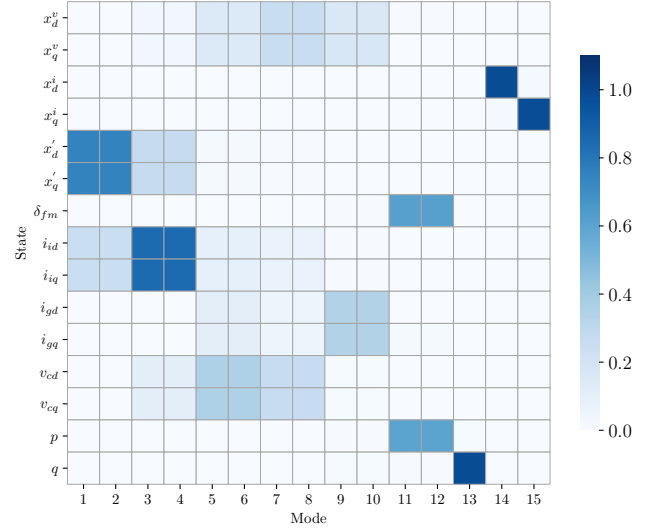


Fig. 6. Participation factors ($p_{k,i}$) for the droop-controlled GFM inverter.

B. Effect of Voltage and Current Regulator Parameters

Last, we explore the effect of the voltage and current regulator parameters on the GFM inverter's small-signal stability. Fig. 7(a) demonstrates the eigenvalue trajectories as we vary K_{p_v} from 0.00015 Ω to 0.1 Ω given $K_\omega = 0.005 \text{ rad/sW}^{-1}$ and $K_\omega = 0.0005 \text{ rad/sW}^{-1}$, respectively. Note that a conjugate pair of eigenvalues moves into the right half-plane (RHP) when $K_{p_v} \approx 0.066 \Omega$. Moreover, given the higher K_ω gain, a conjugate pair of eigenvalues exists at low values of K_{p_v} and moves into the LHP as K_{p_v} progressively increases. Thus, K_{p_v} needs to be set moderately (i.e., not very low, or very high) for larger K_ω values. On the other hand, Fig. 7(b) shows the eigenvalue trajectories as K_{p_i} is varied from 0.00085 A^{-1} to 0.0425 A^{-1} . All eigenvalue trajectories are in the LHP for both values of K_ω considered, which suggests that the proportional gain of the voltage controller K_{p_v} has a more pronounced effect on the GFM inverter's stability.

We now perform a time-domain simulation in PSIM using the averaged inverter model to confirm the assertion that $K_{p_v} > 0.066 \Omega$ yields an unstable system. Fig. 8 considers an initial operating point where $K_{p_v} = 0.04 \Omega$, which is subsequently increased at $t = 2$ s to 0.07 Ω . The unstable behavior manifests in the form of 241 Hz oscillations, which

TABLE III
PARTICIPATION FACTORS FOR GRID-FEEDING AND GRID-FORMING INVERTERS.

Inverter Type	Mode Speed		
	Slow	Moderate	Fast
Forming	i_{dq} (0.85), x'_{dq} (0.75)	v_{cdq} (0.35, 0.27), x_{dq}^v (0.26)	x_{dq}^i (0.50), i_{gdq} (0.34)
Forming + droop	i_{dq} (0.85), x_{dq} (0.75)	v_{cdq} (0.35, 0.27), x_{dq}^v (0.26)	x_{dq}^i (0.98), q (0.98), δ_{fm} (0.62), p (0.60)
Feeding	i_{dq} (1.09), v_{cdq} (1.04), x'_{dq} (0.75)	i_{gq} (1.67), δ_{pll} (1.54), v_{cd} (1.35)	i_{dq}^* (1.18, 2.08), γ_{pll} (1.01), x_{dq}^{PI} (0.49)
Feeding + droop	i_{dq} (1.09), v_{cdq} (1.04), x'_{dq} (0.75)	i_{gq} (1.67), δ_{pll} (1.54), v_{cd} (1.35)	i_{dq}^* (1.18, 2.08), γ_{pll} (1.01), x_{dq}^{PI} (0.49)

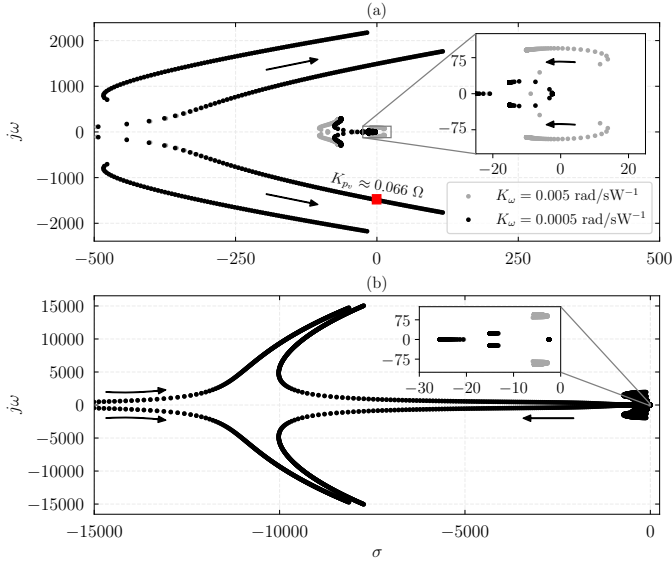


Fig. 7. Eigenvalue trajectories given variations in the voltage and current regulator proportional control gains and the K_ω droop gain. (a) K_{p_v} varied from 0.00015 Ω to 0.1 Ω . (b) K_{p_i} varied from 0.00085 A^{-1} to 0.0425 A^{-1} .

is in good agreement with the predictions of the small-signal model (i.e., $f_{osc} \approx \frac{1518}{2\pi} = 241$ Hz).

IV. CONCLUSION

This paper examined the small-signal modeling and stability of a droop-controlled GFM inverter. Initially, we developed the mathematical model describing the dynamical system. Participation factor analysis demonstrates that the inverter-side current and transport delay states predominantly influence the system's slowest modes. In contrast, the LCL filter states contribute the most to the moderately fast modes, whereas the active power and the SRF angle difference affect the fastest system modes. Comparisons are drawn to grid-feeding inverters, showing that the main modal differences between the two inverter topologies relate to the fastest modes (eigenvalues). Last, small-signal analysis demonstrates that the proportional gain of the voltage regulator can have a more pronounced effect on the GFM inverter's stability compared to the current regulator. Time-domain simulations validate the small-signal model's predictions. The proposed model can be used in practice to characterize stability issues in droop-controlled

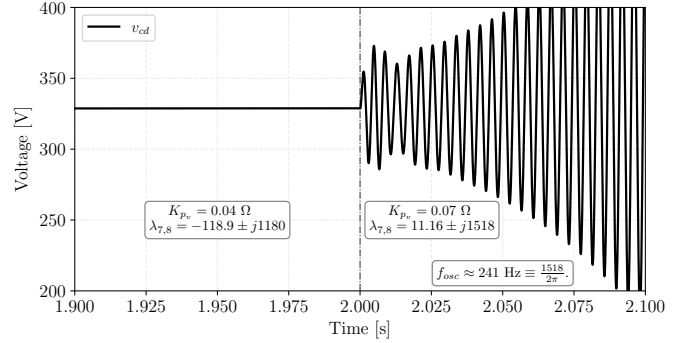


Fig. 8. Time-domain responses of d -axis filter capacitor voltage given a change in K_{p_v} from 0.04 Ω to 0.07 Ω at $t = 2$ s.

GFM inverters accurately. Future work will examine more elaborate GFM functionality.

REFERENCES

- [1] W. Du, Z. Chen, K. P. Schneider, R. H. Lasseter, S. Pushpak Nandanoori, F. K. Tuffner, and S. Kundu, "A comparative study of two widely used grid-forming droop controls on microgrid small-signal stability," *IEEE J. Emerg. Sel. Topics Power Electron.*, vol. 8, no. 2, pp. 963–975, 2020.
- [2] T. Zhang, "Impacts of inverter control strategies on the stability of low-inertia power systems," in *2020 IEEE Power Energy Soc. Gen. Meet. (PESGM)*, 2020, pp. 1–5.
- [3] S. Almutairi, Z. Miao, and L. Fan, "Stability analysis of two types of grid-forming converters for weak grids," *Int. Trans. Electr. Energy Syst.*, 2021.
- [4] S. Eberlein and K. Rudion, "Small-signal stability modelling, sensitivity analysis and optimization of droop controlled inverters in LV micro-grids," *Int. J. Electr. Power Energy Syst.*, vol. 125, 2021.
- [5] J. Kang and K. Hur, "Shaping the transient performance of droop-controlled grid forming converters for frequency regulation," in *2021 IEEE 12th Energy Convers. Congress Expo. - Asia (ECCE-Asia)*, 2021, pp. 1777–1777.
- [6] Y. Li, Y. Gu, Y. Zhu, A. Junyent-Ferré, X. Xiang, and T. C. Green, "Impedance circuit model of grid-forming inverter: Visualizing control algorithms as circuit elements," *IEEE Trans. Power Electron.*, vol. 36, no. 3, pp. 3377–3395, 2021.
- [7] P. Mu, B. McGrath, D. G. Holmes, and C. Teixeira, "Small signal stability analysis of parallel connected grid-tied inverters with direct and self synchronisation of the phase locked loop," in *2020 IEEE Energy Convers. Congr. Expo. (ECCE)*, 2020, pp. 6197–6204.
- [8] G. Tzounas, I. Dassios, and F. Milano, "Modal participation factors of algebraic variables," *IEEE Trans. Power Syst.*, vol. 35, no. 1, pp. 742–750, 2020.
- [9] J. S. Bryant, B. McGrath, L. Meegahapola, and P. Sokolowski, "Small-signal stability analysis of voltage source inverters operating under low short-circuit ratios," in *2021 IEEE Madrid PowerTech*, 2021, pp. 1–6.
- [10] D. G. Holmes, T. A. Lipo, B. P. McGrath, and W. Y. Kong, "Optimized design of stationary frame three phase AC current regulators," *IEEE Trans. Power Electron.*, vol. 24, no. 11, pp. 2417–2426, 2009.